Journal of Materials Chemistry A

PAPER

View Article Online
View Journal | View Issue

Cite this: J. Mater. Chem. A, 2014, 2, 9666

Tin-doped perovskite mixed conducting membrane for efficient air separation

Zhenbao Zhang,[a] Yubo Chen,[ab] Moses O. Tade,[b] Yong Hao,[c] Shaomin Liu[b] and Zongping Shao*[ab]

Received 23rd February 2014
Accepted 23rd April 2014

DOI: 10.1039/c4ta00926f

www.rsc.org/MaterialsA

In this study, we propose a new tin-doped perovskite oxide, $BaCo_{0.7}Fe_{0.2}Sn_{0.1}O_{3-\delta}$ ($BCFSn_{0.1}$), as a promising alternative material for a ceramic oxygen-permeating membrane. A high energy ball milling-assisted solid-state reaction method is used for the material synthesis. The effect of tin doping on the structure, electrical conductivity, oxygen activity, oxygen bulk diffusivity and surface exchange properties of the materials, sintering behaviour, and oxygen permeability of the related membranes is systematically investigated *via* transmission electron microscopy (TEM), environmental scanning electron microscopy (E-SEM), thermo-gravimetric analysis (TGA), oxygen temperature-programmed desorption (O_2-TPD) and electrical conductivity relaxation (ECR), and oxygen permeation test. The minor substitution of B-site cations in $BaCo_{0.7}Fe_{0.3}O_{3-\delta}$ (BCF) with tin is found to be highly effective in improving oxygen flux of the resultant membrane. Under an oxygen gradient created by air/helium, $BCFSn_{0.1}$ membrane reaches fluxes of 9.62×10^{-7} and 3.55×10^{-7} mol m^{-2} s^{-1} Pa^{-1} [STP], respectively, at 900 and 700 °C, in sharp contrast with the flux values of 4.42×10^{-7} and 2.84×10^{-8} mol m^{-2} s^{-1} Pa^{-1} for BCF membrane with the same thickness of 1 mm. Favorable permeation stability is also demonstrated for the tin-doped membrane, and oxygen bulk diffusion is the main rate-limiting step for oxygen permeation, indicating a further increase in fluxes by reducing the membrane thickness.

Introduction

Oxygen permeating ceramic membranes have received considerable attention during the past two decades due to their outstanding features of continuous operation of separating oxygen from air with infinite selectivity, higher permeability compared to the microporous membrane and, in particular, the possibility of providing a cost-effective method for oxygen production for industrial usage. Conventionally, oxygen has a big market as it has been widely used not only in medicine and healthcare but also in industrial applications and combustion, which typically include acid synthesis, steel and iron industry, metal welding process, mining to decompose rocks, waste treatment and chemical combustion. Climate change has further boosted the oxygen business since almost all large-scale clean energy technologies require O_2 as a feed gas. Currently, cryogenic air distillation is the only viable method to produce oxygen from air for industrial-scale applications; however, it is expensive and energy intensive, and thus impedes the deployment of clean energy technologies. In this context, ceramic membrane technology provides a promising alternative, which is exemplified by the big investment in ionic transporting ceramic membrane for air separation by Air Product in USA. In addition to oxygen production, these robust oxygen permeating ceramic membranes can also be used in the oxidative reaction of hydrocarbons to value-added products with greatly reduced emissions or improved selectivity for aimed products.[1–5] Oxygen permeation by dense ceramic membranes occurs *via* ion diffusion mechanism.[6] In such a typical separation process, molecular oxygen from the oxygen-rich side of the atmosphere is first adsorbed on the membrane surface. This is followed by the dissociation of molecular oxygen to oxygen ion and electrons. Then, both charges diffuse through the bulk of the membrane to the other side of membrane surface because of the oxygen partial pressure gradient across the membrane. On the other membrane surface, the oxygen ion and electrons are re-combined to form molecular oxygen and released to the surrounding atmosphere. The successful application of mixed conducting membranes in practice is strongly dependent on several key factors in terms of operational stability, permeation flux, and material cost.

During the past decades, many mixed conducting materials for oxygen permeating membranes have been developed. Most of the materials with high oxygen permeability are categorized as ABO_3 perovskite lattice structures, containing larger alkaline

[a]State Key Laboratory of Materials-Oriented Chemical Engineering, College of Chemistry & Chemical Engineering, Nanjing Tech University, No. 5 Xin Mofan Road, Nanjing, 210009, PR China. E-mail: shaozp@njut.edu.cn; Fax: +86 25 83172242; Tel: +86 25 83172256

[b]Department of Chemical Engineering, Curtin University, WA 6845, Australia

[c]Institute of Engineering Thermophysics, Chinese Academy of Sciences, Beijing 100190, PR China

earth metal element (Ba^{2+}, Sr^{2+}, Ca^{2+}, Ln^{3+}) in the A site and smaller transition metal element (Ni^{x+}, Cu^{x+}, Co^{x+}, Fe^{x+}, Mn^{x+}) in the B site.[7–15] Ba^{2+} is one of the popular dopants for the A site of perovskite because of its low oxidation state (+2, facilitating the formation of oxygen vacancy in the perovskite lattice), large ionic size (increasing the free lattice volume), low metal–oxygen average bond energy (facilitating the oxygen movement inside the lattice), and high basicity (promoting the surface oxygen exchange reactions), while the Co^{x+}/Fe^{x+} couple is often used in the B site, which results in superior performance. Thus, the $BaCo_xFe_{1-x}O_{3-\delta}$ related oxides have been extensively investigated as potential membrane materials for oxygen separation.[16–20]

Perovskite oxides can have several types of lattice structures. Among them, oxygen vacancy disordered cubic structure is preferred since the 3d orbital of B-site cations and 2p orbital of O are highly overlapped, which facilitates the electron hopping and all three dimensions favor the oxygen diffusion. Considering the non-cubic superlattice structure of $BaCo_xFe_{1-x}O_{3-\delta}$ oxides,[17] doping the B-site of $BaCo_xFe_{1-x}O_{3-\delta}$ with other elements to stabilize the oxygen vacancy disordered cubic perovskite lattice structure down to room temperature has been extensively attempted. To date, Zr^{4+}, Ti^{4+}, Nb^{5+}, Bi^{5+}, Ce^{4+}, and Ta^{5+} have been proven to be the successful dopants.[21–26] Among them, Nb^{5+} seems to be the most attractive dopant in terms of oxygen permeability and phase stability of the resultant membranes.[23,27] However, Nb_2O_5, which is used as raw material, is relatively expensive, thus increasing the cost of membrane synthesis. In addition, the high oxidation state of Nb^{5+} will reduce the oxygen vacancy concentration within the perovskite oxide lattice, and the tolerance of Nb^{5+} in perovskite structure is very limited.[28]

An ideal dopant for $BaCo_xFe_{1-x}O_{3-\delta}$ should possess low oxidation state to maximize oxygen vacancy concentration in the perovskite oxide lattice, wide availability with low cost, low metal–oxygen average bond energy to facilitate oxygen diffusion, suitable cation size to match the requirement to form a cubic perovskite, and stable oxidation state to avoid thermal reduction and so on. Given these considerations, Sn^{4+} is a better dopant candidate with a cation size of 0.69 nm when it is in 6 coordination with oxygen. It also has a relatively low metal–oxygen bond energy of 548 kJ mol^{-1}, in comparison with 760, 662 and 753 kJ mol^{-1} for Zr–O, Ti–O, and Nb–O, respectively, and easier sintering because SnO_2 is frequently used as a sintering aid. Sn^{4+} is also advantageous with its lower material cost compared to Nb^{5+} and the good tolerance in a cubic perovskite structure, which can be maintained even for $BaSnO_3$ with the total replacement of B site cation by Sn^{4+}.[29]

In this study, we reported a new perovskite-type oxide as the mixed conducting ceramic membranes for oxygen separation from air. The effects of tin doping on the structure, sintering, electrical conductivity, oxygen activity, oxygen bulk diffusivity, surface exchange properties and oxygen permeability of the resultant membranes were systematically investigated. The tin-doped BCF ($BaCo_{0.7}Fe_{0.2}Sn_{0.1}O_{3-\delta}$, $BCFSn_{0.1}$) showed comparable permeation flux value and stability to state-of-the-art membrane-Nb^{5+} doped BCF ($BaCo_{0.7}Fe_{0.2}Nb_{0.1}O_{3-\delta}$); however, it has better sintering capability and lower cost as compared with $BCFSn_{0.1}$. Therefore, it is a promising material for oxygen supply in future.

Experimental section

Sample fabrication

The $BaCo_{0.7}Fe_{0.3-x}Sn_xO_{3-\delta}$ ($x = 0$, 0.1) powders were prepared by a high energy ball milling-assisted solid-state reaction of the required stoichiometry of $BaCO_3$, Co_3O_4, Fe_2O_3 and SnO_2 (all of analytical grade). Starting raw materials were ball milled (FRITSCH pulverisette 6) in acetone at a rotation speed of 400 rpm for 40 min. After drying, the primary powders were calcined at 950 °C for 5 h in air, followed by calcining at 1100 °C for 10 h in air. The sintered powder was ball milled again for 30 min with ethanol as the milling medium to get qualified uniform powders. The as-obtained oxide powders were then compressed into disk-shaped membranes in a stainless steel mold (15.0 mm in diameter) under hydraulic pressure of approximately 1.5×10^8 Pa. Then, the green disks were sintered in air at 1120 °C for 5 h. The pristine BSCF powder was prepared by the EDTA–citrate complexing method and the membranes were sintered at 1100 °C for 5 h for comparison with $BCFSn_{0.1}$.

Basic characterization

The phase structures of the as-prepared materials were determined by X-ray diffraction (XRD) using a Bruker D8 Advance diffractometer in the range of 2θ from 20° to 80°. Rietveld refinements on the XRD patterns were carried out using GSAS software. An *in situ* high-temperature X-ray diffractometer (HT-XRD, Philips, X'Pert Pro) was utilized to measure the structural evolution of powders across a temperature cycle from room temperature to 1000 °C in air with a heating and cooling rate of 5 °C min^{-1}. The room-temperature oxygen nonstoichiometry was measured by the iodometric titration technique and the oxygen desorption properties of as-prepared materials were investigated by the oxygen temperature-programmed desorption (O_2-TPD) experiment. The thermal reduction capability was comparatively studied by thermo-gravimetric analysis (TGA, Netzsch, STA 449 F3) in air. Note that the pellet was previously sintered for the thermal expansion coefficient (TEC) test. The morphology of the membranes was observed using environmental scanning electron microscopy (ESEM, QUANTA-2000) and the particulate morphology of BCF and $BCFSn_{0.1}$ oxide was examined using transmission electron microscopy (TEM, JEOL JEM-2100).

Oxygen permeation measurement

The oxygen permeation properties of as-prepared disk-shaped membranes were investigated by gas chromatography (GC) using a high-temperature oxygen permeation apparatus. The as-synthesized BCF, $BCFSn_{0.1}$ and BSCF membranes, after being polished on both sides to the thickness of 1.00 mm by 400 mesh SiC abrasive paper, were fixed onto dense alumina with the silver paste used as the sealant. The sidewall of those membranes was also covered with silver to avoid radical

contribution to the oxygen flux. During the oxygen measurement, the temperature was slowly increased to 900 °C at a rate of 5 °C min^{-1} for the oxygen permeation test. Ambient air was applied as the oxygen-rich side atmosphere and helium as the sweep gas with the flow of 100 ml min^{-1} [STP] to create an oxygen partial pressure gradient across the membrane. The oxygen permeation measurement was performed from 700 to 900 °C with a step of 25 °C. Helium also acted as the carrier gas to bring the permeated oxygen to a gas chromatograph (GC, Varian 3800) equipped with a 5 Å capillary molecule column and thermal conductivity detector (TCD) for quantitatively concentration analysis.

The oxygen permeation flux was calculated by:

$$J_{O_2}(\text{ml cm}^{-2}\ \text{min}^{-1},\ \text{STP}) = \left[C_O - C_N \times \frac{0.21}{0.79} \times \left(\frac{28}{32}\right)^{\frac{1}{2}}\right] \times \frac{F}{S} \quad (1)$$

where C_O and C_N are the measured gas-phase concentrations of oxygen and nitrogen in the gas on the sweep side, respectively. F is the flow rate of the exit gas on the sweep side (ml min^{-1}), and S is the membrane geometric surface area of the sweep side (cm^2). $(28/32)^{1/2}$ is the square root of the ratio of N_2 molecular weight *versus* O_2 molecular weight, which is related to the Knudsen diffusion coefficient.

Results and discussion

Phase structure

Fig. 1(a) shows the room-temperature XRD patterns of $BCFSn_{0.1}$ and BCF as synthesized by the mechano-activation promoted solid-state reaction method after the further calcination at 1100 °C. It is well known that perovskite oxides can have several lattice symmetries. For a perovskite oxide with an ideal cubic symmetry, the ionic size of the A-site cation, the B-site cation and the oxygen ion should meet the requirement of $R_A + R_O = \sqrt{2}(R_B + R_O)$, where R_A, R_B and R_O are the ionic radius of A site cation in 12 coordination with oxygen, B site cation in 6 coordination with oxygen, and oxygen ion, respectively. The mismatch in R_A and R_B could introduce large strain within the oxide lattice, resulting in a distortion of the oxide lattice with cubic symmetry or the formation of low symmetry structures. For example, a 2H-$BaNiO_3$ structure was reported for some perovskite oxides having a large size A site cation as compared to the B site cation (for example, $((R_A + R_O)/\sqrt{2}(R_B + R_O)) > 1.03$).[30] Sometimes, the oxygen vacancy ordering within the oxide lattice could also occur, leading to the formation of some superlattice structure.[31] For the undoped BCF parent oxide, the diffraction patterns can be well indexed based on a hexagonal structure, which is a quite common observation for perovskite oxides with a large mismatch in the size of A and B site cations (too large tolerance factor). It should be mentioned that the tolerance factor is closely related to the size of B site cations in BCF, in which cobalt and iron cations have multiple oxidation states and spin states. Interestingly, by partial substitution of only 10% of the B-site cations with Sn^{4+} (here the Sn^{4+} was designed for the partial substitution of Fe^{x+} in BCF), the diffraction patterns changed significantly, and they can be well indexed based on an oxygen vacancy disordered perovskite lattice structure. We then further analyzed the phase structure of BCF and $BCFSn_{0.1}$ by Rietveld refinement with the plots shown in Fig. 1(b) and (c). For the BCF sample, the structure can be refined well based on a hexagonal structure, space group $P\bar{3}m1$ with $a = 5.71$ Å, $b = 5.71$ Å and $c = 11.94$ Å, and $\alpha = \beta = 90°$, $\gamma = 120°$, and the low R ($R_{wp} = 3.75\%$, $R_p = 2.53\%$, $\chi^2 = 3.694$). For the $BCFSn_{0.1}$ sample, the pattern can be refined well based on a cubic symmetry $Pm\bar{3}m$ with $a = b = c = 4.09$ Å, and the low R ($R_p = 2.07\%$, $R_{wp} = 2.97\%$, $\chi^2 = 2.664$) for $BCFSn_{0.1}$, indicating a good fitting.

The crystal structures of both samples were also analyzed by HR-TEM. Fig. 2 shows the corresponding TEM, HR-TEM, SAED and the simulated plots of crystal lattice in the crystalline fringe of image for BCF (Fig. 2(a)–(d)) and $BCFSn_{0.1}$ (Fig. 2(a′)–(d′)). For the BCF sample, the asymmetric SAED patterns agreed with its hexagonal structure as indicated by XRD. The diffraction fringes of distance $d = 0.456$ nm matched pretty well with the distance of (101) fringe plane of the hexagonal structure. For the $BCFSn_{0.1}$ sample, the SAED dots clearly demonstrated a more symmetric array, and the diffraction fringe distance of $d = 0.378$ nm matched well that of (100) diffraction plane for a cubic perovskite.

To demonstrate if the cubic structure after the doping of Sn^{4+} into BCF was metastable, we further conducted the phase structure analysis at different temperatures by HT-XRD in air. During the measurement, the sample was progressively heated up from room temperature to 1000 °C at a rate of 5 °C min^{-1} in air, and the test points of 200, 400, 500, 600, 700, 800, 900 and 1000 °C were selected. At each test point, a stabilization time of 10 min was allowed. After the test at 1000 °C, the temperature was decreased to room temperature in a reverse manner to allow a complete thermal cycle. Fig. 3 shows the related HT-XRD patterns. At each temperature, the $BCFSn_{0.1}$ sample demonstrated the same diffraction pattern, which can be indexed based on a cubic perovskite structure, suggesting the high thermal stability of the oxide after doping. A progressive shift of the diffraction peaks to lower 2θ angle was observed with the increase of temperature, a sign of the lattice expansion, which is related to both thermally induced expansion and chemical expansion from thermal reduction and spin state transition of the B-site cations.

In 6 co-ordination with oxygen, Sn^{4+} attained a cation size of 0.69 nm, which was slightly larger than Fe^{3+} in HS (0.645 nm) and much larger than Fe^{4+} (HS, LS) and Fe^{3+} in LS. Assuming all the Sn^{4+} were substituted by low spin Fe^{4+} while the other cobalt and iron cations in $BCFSn_{0.1}$ had the same valence state and spin state as that in BCF, the difference in tolerance factor between BCF and $BCFSn_{0.1}$ was only 0.0079. Such a small variation in tolerance factor should not result in the big difference in phase structure of BCF and $BCFSn_{0.1}$. Thus, it is likely the Sn^{4+} doping also affected the oxidation state and spin state of the cobalt and iron. The average oxidation of cobalt and iron in BCF and $BCFSn_{0.1}$ was then measured by chemical titration, which turned out to be 3.73 and 3.32, respectively. Indeed, the introduction of Sn^{4+} effectively reduced the oxidation state of Co/Fe in BCF, which facilitated the formation of a cubic perovskite structure since the large Ba^{2+} in the A site requires

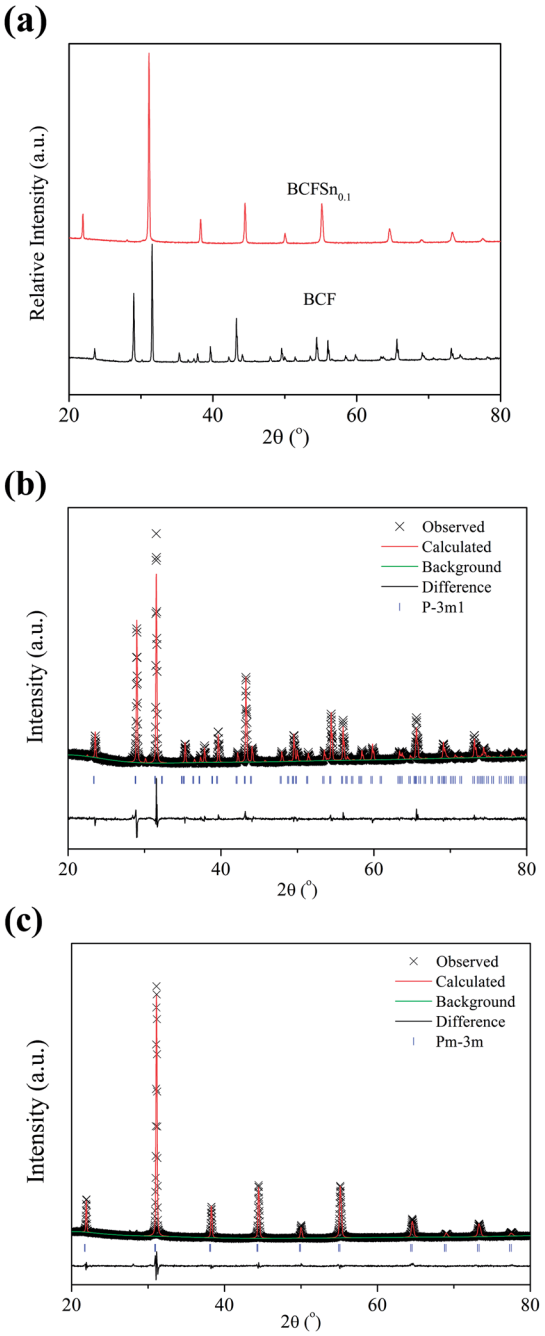

Fig. 1 XRD patterns of BCF and $BCFSn_{0.1}$ powders calcined at 1100 °C for 10 h under air (a), and Rietveld refinement plots of BCF (b) and $BCFSn_{0.1}$ (c).

large cations in the B site to create a proper tolerance factor. However, the effect of Sn^{4+} on the spin state transition of cobalt and iron is not detected in experimental study due to limitations of appropriate apparatus.

Basic properties

An alternative way to stabilize the cubic structure of BCF is to dope the A site (Ba^{2+}) with a cation of smaller size. A typical example is the successful development of $Ba_{0.5}Sr_{0.5}Co_{0.8}Fe_{0.2}O_{3-\delta}$ (BSCF) by partial doping the A-site of $SrCo_{0.8}Fe_{0.2}O_{3-\delta}$ with Ba^{2+},

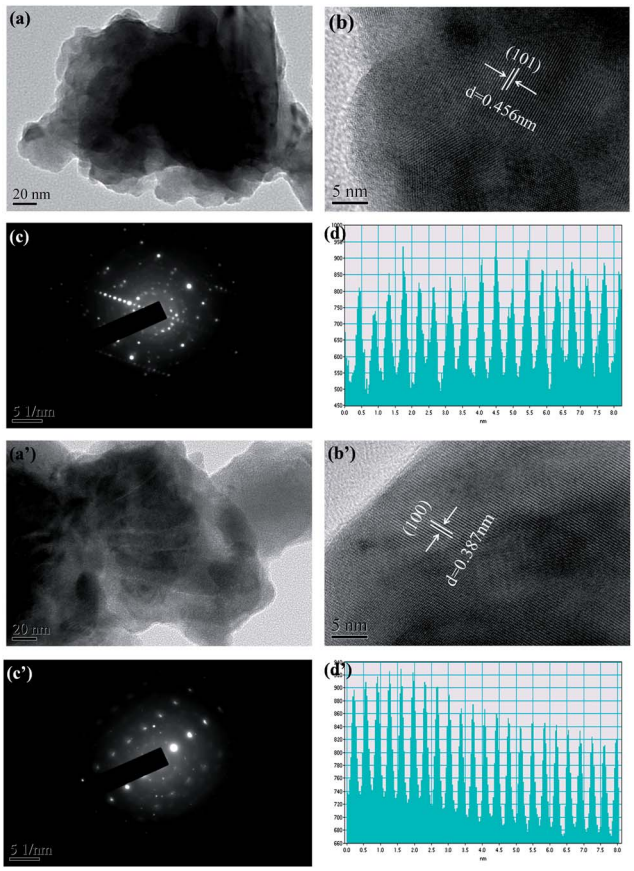

Fig. 2 The corresponding TEM, HR-TEM, SAED and simulated plots of crystal lattice in the crystalline fringe of image for BCF (a–d) and $BCFSn_{0.1}$ (a′–d′).

which is one of the perovskite oxides with the highest oxygen permeability. However, it is well known that BSCF had very large thermal expansion coefficient (TEC), reaching as large as 24×10^{-6} K^{-1},[32] which was contributed from both pure thermal expansion and chemical expansion related to the spin state change and oxygen release/upload due to the partial thermal reduction of the of B-site cations. The large TEC could sometimes introduce large internal stress for the membrane under a large oxygen partial pressure gradient across the membrane, which is detrimental to the integrity of the membrane; thus, a lower TEC is preferred. Fig. 4 shows the thermal expansion curves for BSCF, $BCFSn_{0.1}$ and BCF oxides in air. A large transition at around 470 °C was observed for BSCF, and the TEC calculated for BSCF is 15.5×10^{-6} K^{-1} between room temperature and 400 °C, 22.9×10^{-6} K^{-1} between 470 and 840 °C, and 18×10^{-6} K^{-1} between room temperature and 1000 °C. For the $BCFSn_{0.1}$ sample, the TECs are much smaller, and they are 13.2×10^{-6}, 17.8×10^{-6} and 15.1×10^{-6} K^{-1} correspondingly at the above three temperature zones. However, a large transition at around 620 °C was observed for BCF, and the TEC calculated for BCF is 12.8×10^{-6} K^{-1} between room temperature and 620 °C, 28.1×10^{-6} K^{-1} between 620 and 960 °C, and 18.7×10^{-6} K^{-1} between room temperature and 1000 °C. To get more information about the difference in TECs of the three

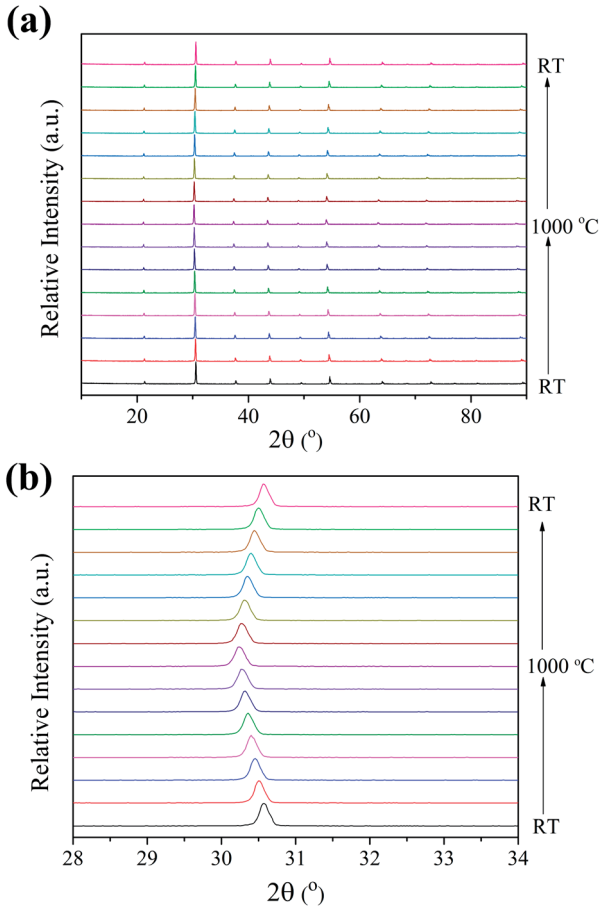

Fig. 3 (a) HT-XRD patterns of $BCFSn_{0.1}$ powder between room temperature and 1000 °C and (b) magnified HT-XRD patterns at 2 theta range from 28° to 34°.

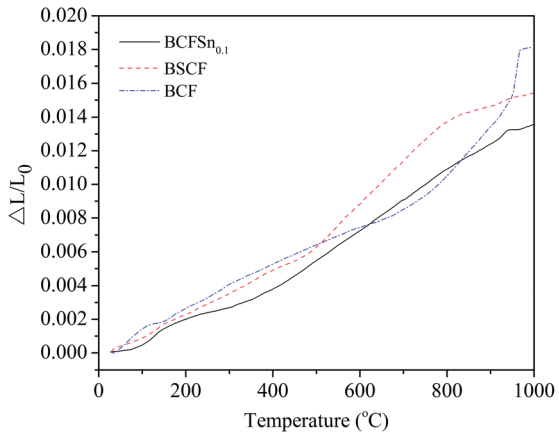

Fig. 4 The thermal expansion curve for BCF, $BCFSn_{0.1}$ and BSCF samples.

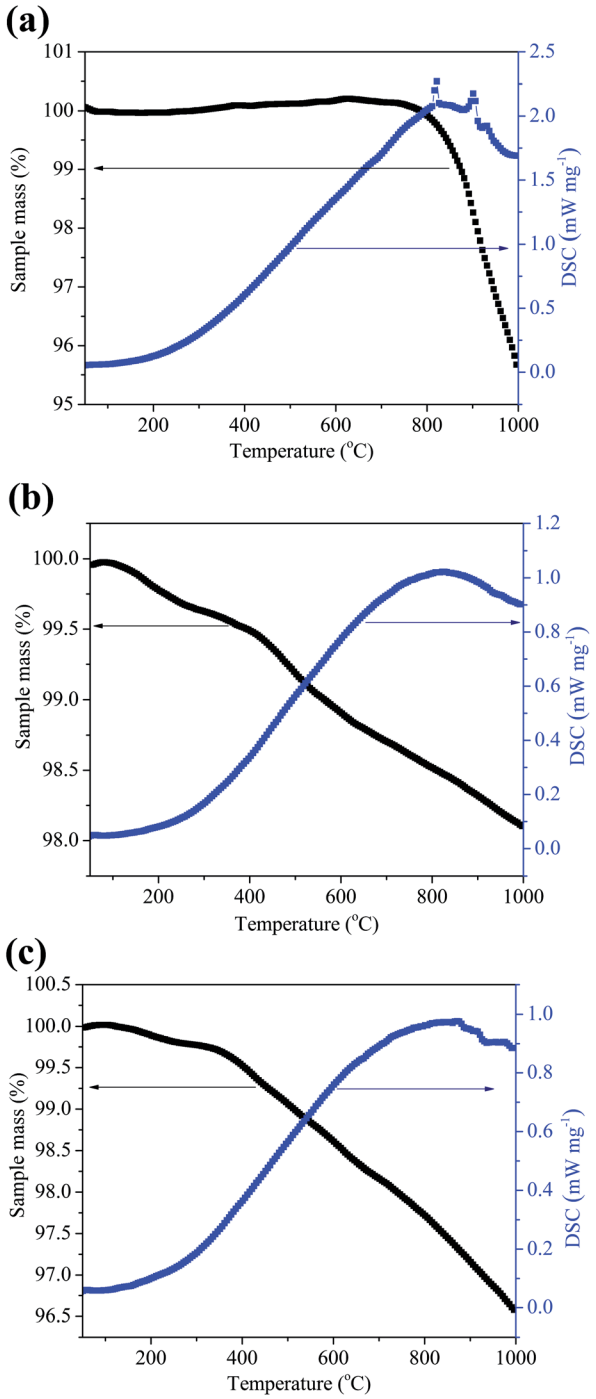

Fig. 5 The TGA curves of BCF (a), $BCFSn_{0.1}$ (b) and BSCF (c).

materials, their thermal reduction capability was comparatively studied by TGA with the results shown in Fig. 5. Note that $BCFSn_{0.1}$ showed weight loss at a low temperature of ~200 °C with almost no abrupt change, while BSCF started to dramatically lose weight at a relatively higher temperature and BCF showed a weight loss from extremely high temperature of ~700 °C. Among these three investigated materials, BCF showed the largest weight loss, while $BCFSn_{0.1}$ had the smallest weight loss. The observed TGA results are consistent with the TEC measurement, in which $BCFSn_{0.1}$ exhibited the lowest TEC values with almost no abrupt change of the slope. The onset temperature of weight loss was closely related to the oxygen mobility, and the total weight loss is related to the reducible capability of the transitional metals in the oxide materials. The

present results suggest that the transitional metals in Sn^{4+}-doped BCF are hard to reduce, which is beneficial for the structure stability, and the oxygen mobility is much faster than the undoped BCF, which is in conformity with the oxygen mobility in hexagonal structure being much more difficult than that in cubic perovskite structure.

Because of the charge diffusion mechanism for the oxygen permeation through mixed conducting membrane, the oxygen permeability is closely related to the oxygen mobility within the oxide lattice. Here, O_2-TPD was applied to get information about the oxygen mobility within the oxide. Fig. 6 shows the O_2-TPD profiles of BSCF and $BCFSn_{0.1}$. For the BSCF oxide, the oxygen release started at around 380 °C, and a large α peak (α peak) was observed between 400 and 700 °C, which is related to the reduction of Fe^{4+}/Co^{4+} to Fe^{3+}/Co^{3+}. At 850–1000 °C, another small O_2 peak (β peak) was also observed, which can be assigned to the reduction of Co^{3+} to Co^{2+}. The much larger α peak of BSCF than $BCFSn_{0.1}$ agrees with the higher reducibility of cobalt and iron in BSCF than in $BCFSn_{0.1}$ as demonstrated by TGA. Interestingly, a lower starting temperature for the oxygen release was observed in $BCFSn_{0.1}$ (~300 °C) than in BSCF (~380 °C). This suggests that the oxygen in $BCFSn_{0.1}$ possibly possessed higher mobility than that in BSCF, especially at lower temperature. We then determined the D_{chem} and k_{chem} values of $BCFSn_{0.1}$ by conductivity relaxation. The sample was first equilibrated at a selected temperature in air to achieve stable conductivity, and then the surrounding atmosphere was suddenly changed to a Ar–O_2 mixture gas with P_{O_2} of 0.1 atm. Thus, a new oxygen vacancy concentration within the oxide lattice started to form. A conductivity relaxation appeared before the oxide reached a new equilibrium of oxygen content with the environment. Based on the conductivity relaxation curve, D_{chem} and k_{chem} could be derived. Fig. 7 shows the conductivity relaxation curves at different temperatures after sudden change of the atmosphere from air to 10% O_2–Ar mixture gas. It was found that a new equilibrium of electrical conductivity was reached in a short time (1.2–6.4 min) after the change in oxygen partial pressure of the surrounding atmosphere, suggesting the high chemical diffusion coefficient and surface chemical exchange constant of the oxide. A higher

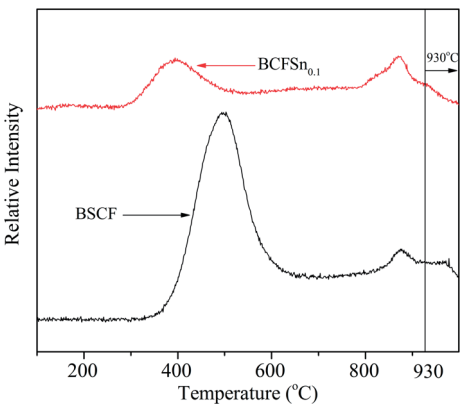

Fig. 6 O_2-TPD profiles of BSCF and $BCFSn_{0.1}$.

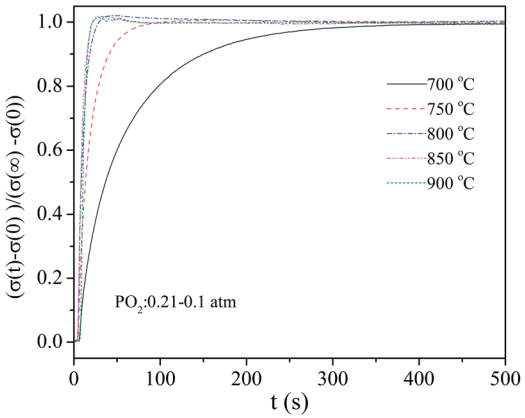

Fig. 7 ECR response curves of $BCFSn_{0.1}$ at various temperatures after sudden change of oxygen partial pressure of the surrounding atmosphere from 0.21 to 0.1 atm.

Table 1 The value of D_{chem} and k_{chem} at different temperatures for $BCFSn_{0.1}$

T (°C)	700	750	800	850	900
$D_{chem} \times 10^4$ (cm^{-2} s^{-1})	1.41	5.22	9.82	10.34	11.98
$k_{chem} \times 10^3$ (cm s^{-1})	1.43	5.91	12.86	12.92	15.39

temperature resulted in a shorter relaxation time, which is in good agreement with the increased surface exchange kinetics and bulk diffusion rate. Table 1 lists the D_{chem} and k_{chem} values at different temperatures for $BCFSn_{0.1}$. A value of 1.03×10^{-3} cm^{-2} s^{-1} was achieved for D_{chem} at 850 °C, which is comparable to that of BSCF, one of the materials with the highest oxygen permeability.[33]

Fig. 8 shows the SEM images of $BCFSn_{0.1}$ sintered at 1120 °C from surface and cross-sectional view; moreover, for comparison, the images of BSCF membrane are also presented (sintering at 1100 °C). Both BSCF and $BCFSn_{0.1}$ membranes were well sintered with large grains of the size of 10–20 μm according to the surface morphology. From the cross-sectional view, the $BCFSn_{0.1}$ membrane was dense with a few isolated pores. As for the BSCF membrane, although it was also well sintered as a whole, some enclosed holes with the diameter of 0.01–3 μm, which is much larger than that in $BCFSn_{0.1}$, were also present. According to TG curves as shown in Fig. 5(b) and (c), BSCF experienced large oxygen release from its oxide lattice during the heating process, and some oxygens were likely enclosed during the sintering process to form enclosed pores in the sintered membranes. It was reported that the enclosed pores could cause detrimental effect on the oxygen permeability of the oxide membrane.[34]

Oxygen permeation performance

The oxygen permeation behavior of the as-fabricated $BCFSn_{0.1}$ membrane was investigated by GC method. Fig. 9 shows the oxygen permeation fluxes through $BCFSn_{0.1}$ membrane with a thickness of 1.0 mm at different temperatures (700–900 °C);

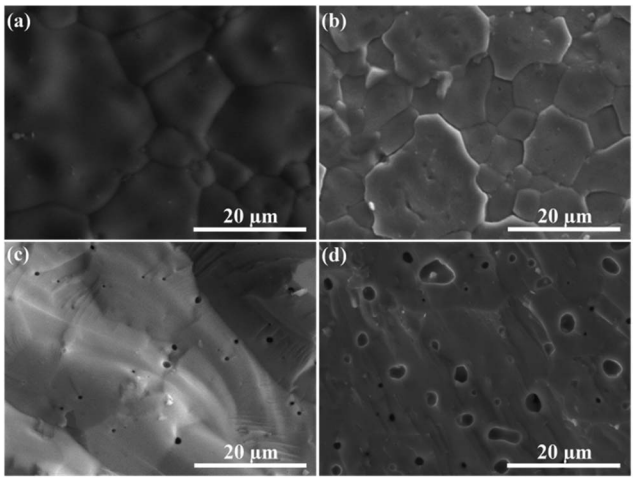

Fig. 8 SEM images of $BCFSn_{0.1}$ (a and c) and BSCF (b and d), where (a) and (b) are from surface views and (c) and (d) are from cross sectional views.

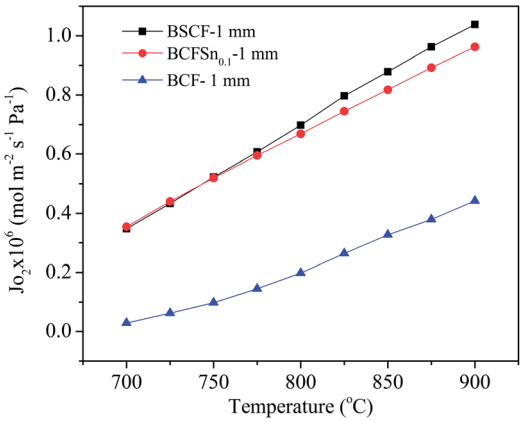

Fig. 9 Temperature dependence of oxygen permeation fluxes through BCF, $BCFSn_{0.1}$ and BSCF membranes.

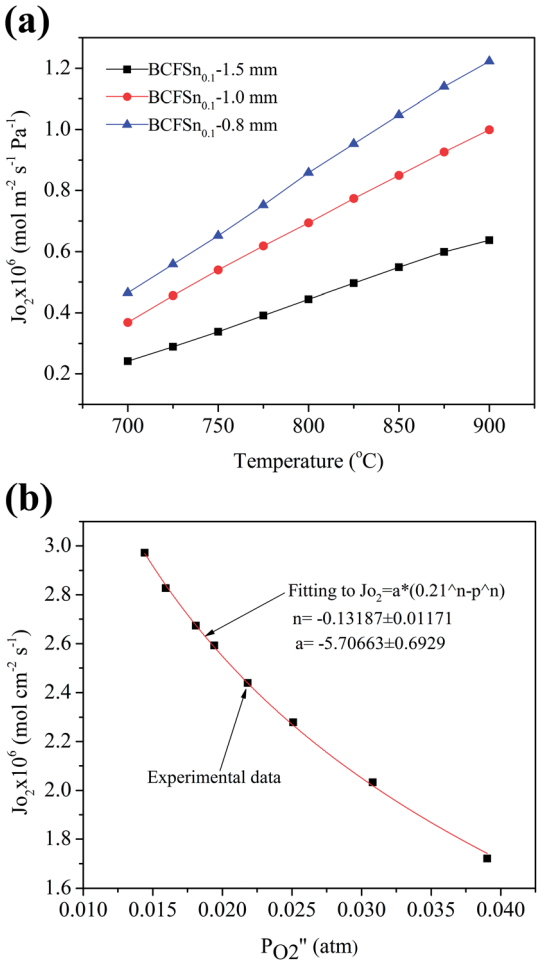

Fig. 10 (a) Temperature dependence of oxygen permeation fluxes through $BCFSn_{0.1}$ membrane with different thicknesses, and (b) the permeation fluxes at 900 °C with different P''_{O_2}.

moreover, for comparison, the permeation fluxes of a BSCF membrane and undoped BCF membrane with the same thickness are also presented. A flux of 9.62×10^{-7} mol m^{-2} s^{-1} Pa^{-1} [STP] was achieved for the $BCFSn_{0.1}$ membrane compared to 1.05×10^{-6} mol m^{-2} s^{-1} Pa^{-1} [STP] for the BSCF membrane. This suggests that the $BCFSn_{0.1}$ membrane had comparable permeability to the BSCF membrane at high temperature. The temperature-related activation energy for oxygen permeation flux of the $BCFSn_{0.1}$ membrane was only 50 kJ mol^{-1} within the temperature range of 700–900 °C compared with 70 kJ mol^{-1} for the BSCF membrane. This suggests that the $BCFSn_{0.1}$ membrane is superior to BSCF membrane for lower temperature operation. For example, at 700 °C, the $BCFSn_{0.1}$ membrane still retained an oxygen permeation flux of 3.55×10^{-7} mol m^{-2} s^{-1} Pa^{-1}, while the permeation flux of BSCF membrane decreased to only 3.32×10^{-7} mol m^{-2} s^{-1} Pa^{-1}. For the undoped BCF membrane, the permeation fluxes are much lower than that of $BCFSn_{0.1}$ and BSCF membranes, and they reached only 4.42×10^{-7} and 2.84×10^{-8} mol m^{-2} s^{-1} Pa^{-1} [STP] at 900 and 700 °C, respectively. This clearly demonstrated the effectiveness of tin doping in improving the permeation performance of the BCF membrane, which can be ascribed to the stabilization of oxygen vacancy disordered cubic structure.

Both the surface exchange and oxygen bulk diffusion could limit the oxygen permeation through a ceramic membrane. Typically, the oxygen surface exchange process has higher activation energy than the oxygen bulk diffusion since the surface process involved oxygen dissociation. The relatively low activation energy for temperature-related oxygen permeation fluxes suggested the oxygen permeation through the $BCFSn_{0.1}$ membrane was likely rate-limited by the ionic bulk diffusion. To get direct information about the controlling step for oxygen permeation through $BCFSn_{0.1}$ membrane, we also tested two membranes with the thickness of 0.8 and 1.5 mm. As shown in Fig. 10(a), a decrease in permeation flux with the increase of membrane thickness was observed. For example, at 900 °C, the permeation fluxes are 1.22×10^{-6}, 9.62×10^{-7} and 6.36×10^{-7} mol m^{-2} s^{-1} Pa^{-1} [STP] for the membranes with the thickness of 0.8 mm, 1.0 mm and 1.5 mm, respectively. The $J_{O_2} \times d$ (mol m^{-2} s^{-1} Pa^{-1} mm) for the three membranes are

9.76×10^{-7} ($d = 0.8$ mm), 9.62×10^{-7} ($d = 1.0$ mm) and 9.54×10^{-7} ($d = 1.5$ mm) at 900 °C. Similar values for all three membranes of different thickness strongly supports that the oxygen permeation through the thick $BCFSn_{0.1}$ membranes was mainly controlled by the oxygen bulk diffusion. According to the Wagner equation, the oxygen permeation flux can be expressed as

$$J_{O_2} = -\frac{RT}{4^2F^2L}\int_{\ln P'_{O_2}}^{\ln P''_{O_2}} \sigma_{ion} d(\ln P_{O_2}), \quad (2)$$

and the oxygen ion conductivity can be expressed as

$$\sigma_{ion} = \sigma^{O}_{ion} P^{n}_{O_2} \quad (3)$$

in relation to oxygen partial pressure of the atmosphere, where L is the thickness of the membrane, P'_{O_2} and P''_{O_2} are the oxygen partial pressures of the oxygen-rich and oxygen-lean sides, respectively, and σ^{O}_{ion} is the oxygen ion conductivity in the standard condition. The Wagner equation suggests that under an oxygen bulk diffusion controlling process, the J_{O_2} should be in power relation to P''_{O_2} with n of negative value, while it is in a positive value if the permeation was controlled mainly by surface exchange process. We then further studied the oxygen permeation through a $BCFSn_{0.1}$ membrane with a thickness of 0.6 mm by fixing the feed-side atmosphere of ambient air and sweep-side atmosphere of helium with different flow rates to create different oxygen partial pressures. Fig. 10(b) shows the permeation fluxes at 900 °C with different P''_{O_2}. The fluxes can be fitted to an experimental power equation of $J_{O_2} = aP''^{n}_{O_2}$ with $R = 0.9991$. The obtained values are $a = -5.707$ and $n = -1.319$. The negative value of n further supported the oxygen bulk diffusion controlling for the oxygen permeation through $BCFSn_{0.1}$ membrane. A reduction in the membrane thickness should lead to a further increase in the permeation flux.

To get information about the permeation stability of the $BCFSn_{0.1}$ membrane, it was tested under the condition of ambient air as feed-side atmosphere and helium at a flow rate of 100 ml min^{-1} [STP] as the sweep gas for a long period. Fig. 11 shows the time dependence of permeation flux through the membrane at 850 °C. During the first 40 h, a slow decrease in permeation flux from an initial value of 8.64×10^{-7} mol m^{-2} s^{-1} Pa^{-1} [STP] to about 7.69×10^{-7} mol m^{-2} s^{-1} Pa^{-1} [STP] at 40 h was observed, it further reduced to 7.16×10^{-7} mol m^{-2} s^{-1} Pa^{-1} [STP] at 100 h, and then the flux remained stable even after the test up to 145 h when the permeation study was stopped. Both sides of the tested membrane were examined by XRD to get information about the cause for the initial decrease in permeation flux. As shown in Fig. 12, some phase transitions were observed at both sides of the membranes. It is common for most perovskite oxide membranes under the condition of presence of oxygen to have a partial pressure gradient across the membrane. Moreover, the basic perovskite structure was maintained for both sides, although the impurity phase at the air side is more significant. Interestingly, such impurity phases could not be indexed based on the potential carbonates. It is likely that phase transition occurred, leading to the formation of some superlattice structure, which cannot be indexed based on well-known oxides. This suggests that the $BCFSn_{0.1}$ was more stable under a lower-oxygen-partial pressure atmosphere. Moreover, after the initial phase transition, a stable permeation flux was maintained, suggesting that the superlattice still possesses oxygen-ion conductivity, although the membrane should have lower oxygen permeability than $BCFSn_{0.1}$.

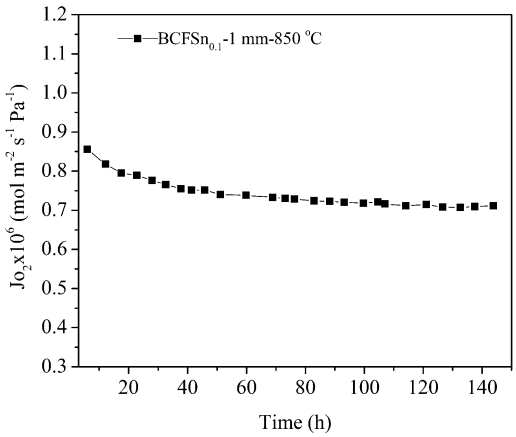

Fig. 11 The time dependence of permeation flux through the $BCFSn_{0.1}$ membrane at 850 °C.

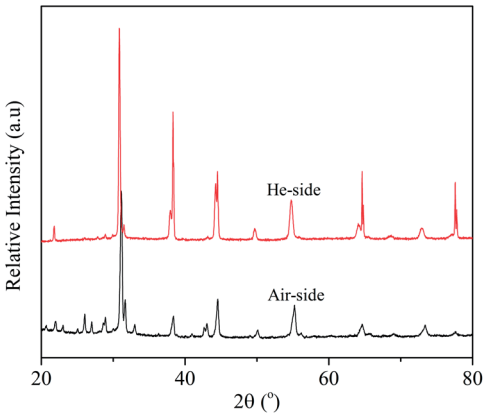

Fig. 12 XRD patterns of the $BCFSn_{0.1}$ membrane from both surfaces after 145 h of permeation study at 850 °C.

Conclusions

$BaCo_{0.7}Fe_{0.3-x}Sn_xO_{3-\delta}$ ($x = 0$, 0.1) oxides were prepared by a mechano-activation promoted solid-state reaction method and investigated as potential materials for air separation ceramic membranes. A partial substitution of only 10% of Fe^{x+} in BCF had a significant effect on the phase structure, sintering behaviour, electrical conductivity, oxygen activity, oxygen bulk diffusivity and surface exchange properties, and the oxygen permeability of the resultant membranes. Under an air/helium gradient, the permeation flux through a 1 mm thick $BCFSn_{0.1}$ membrane reached 9.62×10^{-7} and 3.55×10^{-7} mol m^{-2} s^{-1} Pa^{-1} [STP] at 900 and 700 °C, respectively, which is higher than the permeation flux through a 1 mm thick BCF membrane. The

oxygen permeation flux through the $BCFSn_{0.1}$ membrane was rate-limited by ionic bulk diffusion within the thickness range of 0.6–1.5 mm. The decrease of membrane thickness was an effective way to further improve the oxygen permeation flux.

Acknowledgements

The authors acknowledge the financial support from ARC *via* future fellowship under contract FT100100134. Prof. Yong Hao acknowledges the Recruitment Program of Global Experts of China for funding support.

Notes and references

1 K. Zhang, J. Sunarso and Z. Shao, *RSC Adv.*, 2011, **1**, 1661.
2 Z. P. Shao, W. S. Yang, Y. Cong, H. Dong, J. H. Tong and G. X. Xiong, *J. Membr. Sci.*, 2000, **172**, 177.
3 Y. Teraoka, H. Zhang, K. Okamoto and N. Yamazoe, *Mater. Res. Bull.*, 1988, **23**, 51.
4 X. Shao, D. Dong and G. Parkinson, *J. Mater. Chem. A*, 2013, **1**, 9641.
5 A. Thursfield and I. S. Metcalfe, *J. Mater. Chem.*, 2004, **14**, 2475.
6 Z. B. Rui, Y. D. Li and Y. S. Lin, *Chem. Eng. Sci.*, 2009, **64**, 172.
7 F. F. Dong, D. J. Chen, Y. B. Chen, Q. Zhao and Z. P. Shao, *J. Mater. Chem.*, 2012, **22**, 15071.
8 V. V. Kharton, A. A. Yaremchenko, A. P. Viskup, M. V. Patrakeev, I. A. Leonidov, V. L. Kozhevnikov, F. M. Figueiredo, A. L. Shaulo, E. N. Naumovich and F. M. B. Marques, *J. Electrochem. Soc.*, 2002, **149**, E125.
9 P. Y. Zeng, R. Ran, Z. H. Chen, H. X. Gu, Z. P. Shao, J. C. Diniz da Costa and S. M. Liu, *J. Membr. Sci.*, 2007, **302**, 171.
10 F. Liang, K. Partovi and H. Jiang, *J. Mater. Chem. A*, 2013, **1**, 746.
11 T. Kida, A. Yamasaki, K. Watanabe, N. Yamazoe and K. Shimanoe, *J. Solid State Chem.*, 2010, **183**, 2426.
12 F. F. Dong, Y. B. Chen, R. Ran, D. J. Chen, M. O. Tadé, S. M. Liu and Z. P. Shao, *J. Mater. Chem. A*, 2013, **1**, 9781.
13 K. Efimov, T. Halfer, A. Kuhn, P. Heitjans, J. Caro and A. Feldhoff, *Chem. Mater.*, 2010, **22**, 1540.
14 V. V. Kharton, V. N. Tikhonovich, S. B. Li, E. N. Naumovich, A. V. KovaIevsk, A. P. Visku, I. A. Bashmakov and A. A. Yaremchenko, *J. Electrochem. Soc.*, 1998, **145**, 1363.
15 V. V. Kharton, A. P. Viskup and A. V. Kovalevsky, *J. Mater. Chem.*, 2000, **10**, 1161.
16 P. J. Shen, X. Liu, H. H. Wang and W. Z. Ding, *J. Phys. Chem. C*, 2010, **114**, 22338.
17 H. L. Zhao, N. S. Xu, Y. F. Cheng, W. J. Wei, N. Chen, W. Z. Ding, X. G. Lu and F. S. Li, *J. Phys. Chem. C*, 2010, **114**, 17975.
18 O. Czuprat, M. Arnold, S. Schirrmeister, T. Schiestel and J. Caro, *J. Membr. Sci.*, 2010, **364**, 132.
19 Y. F. Cheng, H. L. Zhao, D. Q. Teng, F. S. Li, X. G. Lu and W. Z. Ding, *J. Membr. Sci.*, 2008, **322**, 484–490.
20 X. Z. Chen, H. F. Liu, Y. Y. Wei, J. Caro and H. H. Wang, *J. Alloys Compd.*, 2009, **484**, 386.
21 J. H. Tong, W. S. Yang, B. C. Zhu and R. Cai, *J. Membr. Sci.*, 2002, **203**, 175.
22 J. H. Tong, W. S. Yang, R. Cai, B. C. Zhu and L. W. Lin, *Mater. Lett.*, 2002, **56**, 958.
23 J. X. Yi, J. Brendt, M. Schroeder and M. Martin, *J. Membr. Sci.*, 2012, **387–388**, 17.
24 Z. P. Shao, G. X. Xiong, Y. Cong and W. S. Yang, *J. Membr. Sci.*, 2000, **164**, 167.
25 Q. M. Li, X. F. Zhu and W. S. Yang, *Mater. Res. Bull.*, 2010, **45**, 1112.
26 J. Z. Liu, H. W. Cheng, B. Jing, X. G. Lu and W. Z. Ding, *Int. J. Hydrogen Energy*, 2013, **38**, 11090.
27 S. D. Song, P. Zhang, M. F. Han and S. C. Singhal, *J. Membr. Sci.*, 2012, **415–416**, 654.
28 K. Zhang, R. Ran, L. Ge, Z. P. Shao, W. Q. Jin and N. P. Xu, *J. Membr. Sci.*, 2008, **323**, 436.
29 C. P. Udawatte, M. Kakihana and M. Yoshimura, *Solid State Ionics*, 1998, **108**, 23.
30 J. C. Grenier, L. Fournès, M. Pouchard and P. Hagenmuller, *Mater. Res. Bull.*, 1986, **21**, 441.
31 H. Shiiba, M. Nakayama, T. Kasuga, R. W. Grimes and J. A. Kilner, *Phys. Chem. Chem. Phys.*, 2013, **15**, 10494.
32 W. Zhou, R. Ran, Z. P. Shao, W. Q. Jin and N. P. Xu, *J. Power Sources*, 2008, **182**, 24.
33 D. J. Chen and Z. P. Shao, *Int. J. Hydrogen Energy*, 2011, **36**, 6948.
34 D. M. Gao, J. Zhao, W. Zhou, R. Ran and Z. P. Shao, *J. Membr. Sci.*, 2011, **366**, 203.

